

# One-pot facile co-precipitation synthesis of the layered $\text{Li}_{1+x}(\text{Mn}_{0.6}\text{Ni}_{0.2}\text{Co}_{0.2})_{1-x}\text{O}_2$ as cathode materials with outstanding performance for lithium-ion batteries

Shaomeng Ma<sup>1</sup> · Xianhua Hou<sup>1,2</sup> · Zanrui Lin<sup>1</sup> · Yanling Huang<sup>1</sup> · Yumei Gao<sup>3</sup> · Shejun Hu<sup>1,2</sup> · Jiadong Shen<sup>1</sup>

Received: 26 January 2015 / Revised: 8 July 2015 / Accepted: 3 August 2015 / Published online: 16 August 2015  
© Springer-Verlag Berlin Heidelberg 2015

**Abstract** The Li-rich layered  $\text{Li}_{1+x}(\text{Mn}_{0.6}\text{Ni}_{0.2}\text{Co}_{0.2})_{1-x}\text{O}_2$  ( $x = 0.14, 0.165, 0.19$ ) cathode materials have been successfully synthesized through a one-pot facile co-precipitation route. The synthesized  $\text{MCO}_3$  ( $\text{M} = \text{Mn}_{0.6}\text{Ni}_{0.2}\text{Co}_{0.2}$ ) precursor mixing with  $\text{Li}_2\text{CO}_3$  was annealed at 500 °C and calcinated at 900 °C. The morphology and structure of the samples were characterized by X-ray diffraction (XRD), scanning electron microscopy (SEM), and transmission electron microscopy (TEM). The results indicate that the sample  $\text{Li}_{1.165}\text{Mn}_{0.501}\text{Ni}_{0.167}\text{Co}_{0.167}\text{O}_2$  ( $x = 0.165$ ) exhibits the most outstanding electrochemical performance, which may be ascribed to uniform particle size and high crystallinity. It delivers an initial discharge-specific capacity of approximately 241.7 mAh  $\text{g}^{-1}$  with an initial coulombic efficiency of 70.3 % at a constant density of 25 mA  $\text{g}^{-1}$ . A reversible discharge-specific capacity of approximately 207.2 mAh  $\text{g}^{-1}$  is still obtained after 100 cycles. The discharge capacities of nearly 226.8, 194.4, 158.9, 143.7, 116.8, 97.5, and 47.6 mAh  $\text{g}^{-1}$  can also be attained under 0.1 C, 0.2 C, 0.5 C, 1 C, 2 C, 5 C, and 10 C (1 C = 250 mA  $\text{g}^{-1}$ ), respectively. The Li-rich layered  $\text{Li}_{1.165}\text{Mn}_{0.501}\text{Ni}_{0.167}\text{Co}_{0.167}\text{O}_2$  will

be a promising cathode material for advanced lithium-ion batteries.

**Keywords** Lithium-ion batteries · Li-rich cathode · Co-precipitation ·  $\text{Li}_{1+x}(\text{Mn}_{0.6}\text{Ni}_{0.2}\text{Co}_{0.2})_{1-x}\text{O}_2$

## Introduction

In the contemporary of attaching great importance to green initiative and energy saving, rechargeable lithium-ion batteries have attracted much attention in the commercial applications of electric vehicles (EVs) and hybrid electric vehicles (HEVs) by virtue of their high energy density, high working voltage, no memory effect, long cycle life, and environmental benignity [1–7]. Notoriously, the cathode with low capacity and high cost makes the development of lithium-ion batteries hit a bottleneck (limits). Thus, searching for advanced cathode materials with excellent performance has been on the top of agenda and the focus of research in the field of lithium-ion batteries in recent years [8–11].

Currently,  $\text{LiCoO}_2$  is still the dominant cathode materials in the business market. Nonetheless, much effort has been made to explore an alternative cathode material to substitute for  $\text{LiCoO}_2$  on account of its toxicity, high cost, and insecurity [12, 13]. In this regard, Li-rich layered cathodes written as  $\text{Li}_{1+x}[\text{M}]_{1-x}\text{O}_2$  ( $\text{M} = \text{Mn}, \text{Ni}, \text{Co}, \text{etc.}; 0 < x < 1$ ) have captured worldwide attention and interests, being a promising candidate for the novel cathode materials of lithium-ion batteries. This type of cathode material is also considered to be a nano-dimensional solid solution with rock salt structure between  $\text{Li}_2\text{MnO}_3$  ( $C2/m$  space group) [14, 15] and  $\text{LiMO}_2$  ( $R-3m$  space group) [16] at different proportions, which is also formulated as  $x\text{Li}_2\text{MnO}_3 \cdot (1-x)\text{LiMO}_2$  [17, 18]. The  $\text{Li}_2\text{MnO}_3$  component is conducive to stabilize the structure

✉ Xianhua Hou  
houxh@scnu.edu.cn

<sup>1</sup> Guangdong Provincial Key Laboratory of Quantum Engineering and Quantum Materials, School of Physics and Telecommunication Engineering, South China Normal University, Guangzhou 510006, China

<sup>2</sup> Engineering Research Center of Materials and Technology for Electrochemical Energy Storage (Ministry of Education), Guangzhou 510006, China

<sup>3</sup> Zhongshan Institute, University of Electronic Science and Technology, Zhongshan 528400, China

and improve the cycling performance. These materials display a unique framework of layered-layered structure, delivering a markedly high specific capacity of over 250 mAh g<sup>-1</sup> in a wide voltage window of 2.0 to 4.8 V as compared to common cathodes [19–21]. Wang et al. [22] prepared Li<sub>1+x</sub>Ni<sub>1/6</sub>Co<sub>1/6</sub>Mn<sub>4/6</sub>O<sub>2.25+x/2</sub> (0.1 ≤ x ≤ 0.7) cathode materials using a simple carbonate co-precipitation route, devoting to researching the structure, morphology, and electrochemical properties detailedly. Min et al. [23] adopted an electrospinning technique with different polymers to discuss the morphological effects on the electrochemical performance, leading to the formation of a fiber and flower-like nano-structured morphology and splendid performance. A hierarchical micro/nano-structured Li-rich layered 0.5Li<sub>2</sub>MnO<sub>3</sub> · 0.5LiMn<sub>0.4</sub>Ni<sub>0.3</sub>Co<sub>0.3</sub>O<sub>2</sub> materials obtained by Fu et al. [24] via a solvothermal method can still maintain a high-valued discharge capacity of 163.3 mAh g<sup>-1</sup> when the rate is increased to 10 C (1 C = 200 mA g<sup>-1</sup>).

Despite the mentioned merits, these integrated materials suffer some unsolved drawbacks, such as low rate capabilities, large irreversible capacity fading, and poor conductivity. Aiming at solving these issues, some strategies, such as surface modification (coating with the positive materials, like carbon [20], oxides, phosphates [6], fluorides [25], etc.), doping [26] with conductive elements, ion substitution [27], or reduction in particle size, have been employed to optimize the morphology and improve the conductivity and cycle stability [23]. Zhang et al. [28] propose a PO<sub>4</sub><sup>3-</sup> polyanion doping for stabilizing the energy density of Li-rich layered Li(Li<sub>0.17</sub>Ni<sub>0.20</sub>Co<sub>0.05</sub>Mn<sub>0.58</sub>)O<sub>2</sub> oxides, minimizing the local structure change and presenting excellent energy density retention. Lithium-rich layered Li[Li<sub>0.2</sub>Mn<sub>0.54</sub>Ni<sub>0.13</sub>Co<sub>0.13</sub>]O<sub>2</sub> was prepared by Xue et al. [29] through integrating a fast co-precipitation method with polyaniline modification, presenting a high rate capacity of 198.6 mAh g<sup>-1</sup> at 10 C. Hou et al. [30] have synthesized festoon-like Li<sub>1.13</sub>[Ni<sub>0.233</sub>Mn<sub>0.534</sub>Co<sub>0.233</sub>]<sub>0.87</sub>O<sub>2</sub> cathode materials with higher capacity and superior rate capability by adopting hexadecyl trimethyl ammonium bromide (CTAB) as a surfactant, which effectively alleviate the layered/spinel structure change during cycling. As a matter of fact, lithium content is also a key factor, having great impact on the morphology and electrochemical properties of cathode materials. Lithium content has an effect on the Li<sup>+</sup> insertion/extraction during the charging-discharging process, thereby influencing the subsequent high-temperature sintering process. Theoretically, the excess of lithium is required due to the Li volatilization in the reaction process. But in fact, metal ions are inevitably wasted to some extent in the experimental early stage, corresponding to the increase of the proportion of lithium in disguise.

In this work, the Li-rich layered Li<sub>1+x</sub>(Mn<sub>0.6</sub>Ni<sub>0.2</sub>Co<sub>0.2</sub>)<sub>1-x</sub>O<sub>2</sub> (x = 0.14, 0.165, 0.19) cathode materials were successfully

synthesized via one-pot facile co-precipitation route and a subsequent calcination procedure. Here, the valence states of manganese, nickel, and cobalt are +4, +2, and +3, respectively [31–34]. What is more, it should be pointed out that the co-precipitation method has many distinct advantages, such as simple process, controllable conditions, short synthesizing cycle, high yield, low cost, and so on, which is much popular and widely applied. Herein, the influence of lithium content on the morphology and electrochemical properties of the batteries was briefly but systematically investigated. The carbonate precursor showed an excellent spherical shape with uniform particle size. The Li<sub>1.165</sub>Mn<sub>0.501</sub>Ni<sub>0.167</sub>Co<sub>0.167</sub>O<sub>2</sub> (x = 0.165) cathode material has an integrated structure and thus exhibits outstanding electrochemical performance. A high discharge-specific capacity of 241.7 mAh g<sup>-1</sup> was acquired in the initial charge-discharge cycling at a current density of 25 mA g<sup>-1</sup>. Moreover, the discharge capacity of 213.5 mAh g<sup>-1</sup> is still remained after 100 cycles. Such excellent performance is mainly due to the uniform and small particle size, which is in favor of the Li<sup>+</sup> extraction/insertion during the charge/discharge process.

## Experimental

### Synthesis of LMNCO materials

All chemicals (Sigma Aldrich) were of commercially available analytical grade and were used without further purification. Li<sub>1+x</sub>(Mn<sub>0.6</sub>Ni<sub>0.2</sub>Co<sub>0.2</sub>)<sub>1-x</sub>O<sub>2</sub> (x = 0.14, 0.165, 0.19) cathode materials were synthesized via one-pot facile co-precipitation method and two-step calcinations subsequently. 1.0 mol L<sup>-1</sup> metal acetate salt solutions (Mn(CH<sub>3</sub>COO)<sub>2</sub> · 4H<sub>2</sub>O, Ni(CH<sub>3</sub>COO)<sub>2</sub> · 4H<sub>2</sub>O, and Co(CH<sub>3</sub>COO)<sub>2</sub> · 4H<sub>2</sub>O in a stoichiometric ratio of 3:1:1) and 1.0 mol L<sup>-1</sup> Na<sub>2</sub>CO<sub>3</sub> solutions were simultaneously pumped into the NH<sub>4</sub>HCO<sub>3</sub> solutions (0.3 mol L<sup>-1</sup>) in a continuous stirred reactor with a stirring speed of 800 rpm. After stirring for 6 h, the obtained precipitation was filtered, rinsed thoroughly with deionized water, and then dried at 60 °C overnight in a vacuum oven. Afterwards, the obtained manganese-nickel-cobalt carbonate precursor was thoroughly mixed with Li<sub>2</sub>CO<sub>3</sub> in stoichiometric amounts. After thorough grinding, the mixture was annealed at 500 °C for 5 h and then calcinated at 900 °C for 12 h in air atmosphere. The final materials were gained by quenching them to room temperature and ground for the fabrication of the electrode.

### Material characterization

The phase analysis of the as-prepared products were characterized by X-ray diffraction (XRD; PANalytical X'Pert PRO, Cu Kα radiation, λ = 0.15406 nm) with Cu Kα radiation in a 2θ range from 10° to 80° at a scan rate of 5°min<sup>-1</sup>. The particle

morphology and crystalline structure of the as-prepared products were performed by scanning electron microscopy (SEM; ZEISS ULTRA 55) and transmission electron microscopy (TEM; JEM-2100HR), accompanying with the high resolution transmission electron microscopy (HRTEM).

### Electrochemical performance test

The electrochemical performance was carried out using coin-type half cells (CR2430) assembled in an argon-filled glove box. The working electrodes were made by casting the slurry with the composition of 80 wt% active materials, 10 wt% Super-P (conductive agent), and 10 wt% PVDF (the binder). The slurry was coated on aluminum foil with thickness of about 10  $\mu\text{m}$  and then dried at 60  $^{\circ}\text{C}$  for 12 h in a vacuum. Subsequently, the electrodes were pressed and punched ( $\phi = 18$  mm), while the metallic lithium foil served as the counter and reference electrodes. 1.0 mol L<sup>-1</sup> LiPF<sub>6</sub> dissolved in ethylene carbonate (EC)—diethyl carbonate (DEC)—ethylene methyl carbonate (EMC) (1:1:1 in volume) was used as the electrolyte and a polypropylene microporous film (Cellgard 2400) as the separator.

The charge-discharge tests were galvanostatically performed on a LAND battery program-control test system between 2.0 and 4.65 V at the charge-discharge rates from 0.1 C to 10 C (1 C = 250 mA g<sup>-1</sup>) at room temperature. Electrochemical impedance spectroscopy (EIS) of the cells was conducted with a frequency range from 10<sup>5</sup> to 0.01 Hz at a complete charge state. Cyclic voltammograms (CV) were carried out on an electrochemical workstation (Solartron Analytical 1470E) in the potential window of 2.5–4.65 V. The potentials in this work are in reference to the Li/Li<sup>+</sup> couple.

### Results and discussion

The Li-rich layered cathode  $x\text{Li}_2\text{MnO}_3 \cdot (1-x)\text{LiMn}_{1/3}\text{Ni}_{1/3}\text{Co}_{1/3}\text{O}_2$  is a nano-dimensional solid solution between monoclinic layered  $\text{Li}_2\text{MnO}_3$  with  $C2/m$  space group [14, 15] and rhombohedral  $\text{LiMO}_2$  with  $R-3m$  space group [16]. The atomic radius of Mn, Ni, and Co is very close to each other, which has little influence on the crystal structure. The XRD patterns of the precursor and samples are shown in Fig. 1. As can be seen from the XRD patterns of the precursor in Fig. 1a, the peaks are almost in accordance with the PDF card of  $\text{MnCO}_3$  (PDF#44–1472), but deviate seriously from that of  $\text{NiCO}_3$  (PDF#12–0771) and  $\text{CoCO}_3$  (PDF#11–0692). That is because the ratio of the amount of Mn, Ni, and Co is fixed at 3:1:1 in our study. Comparatively speaking, the amount of Mn is relatively higher than that of Ni and Co. Besides, it illustrates the precursor is a kind of carbonate. Figure 1b shows the XRD patterns of the active materials. The diffraction peaks except for the low intensity part within

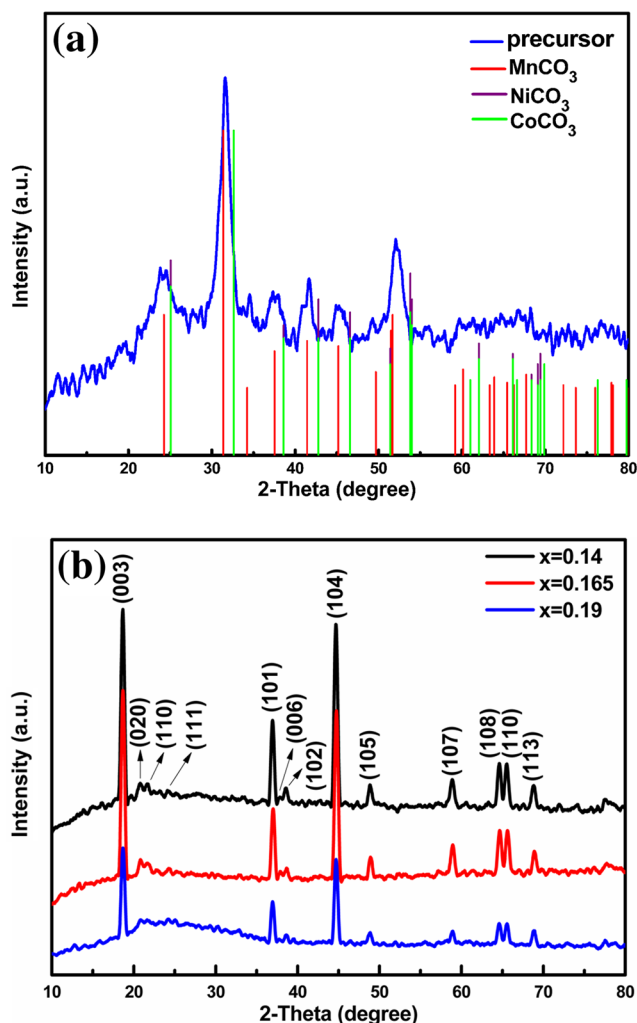


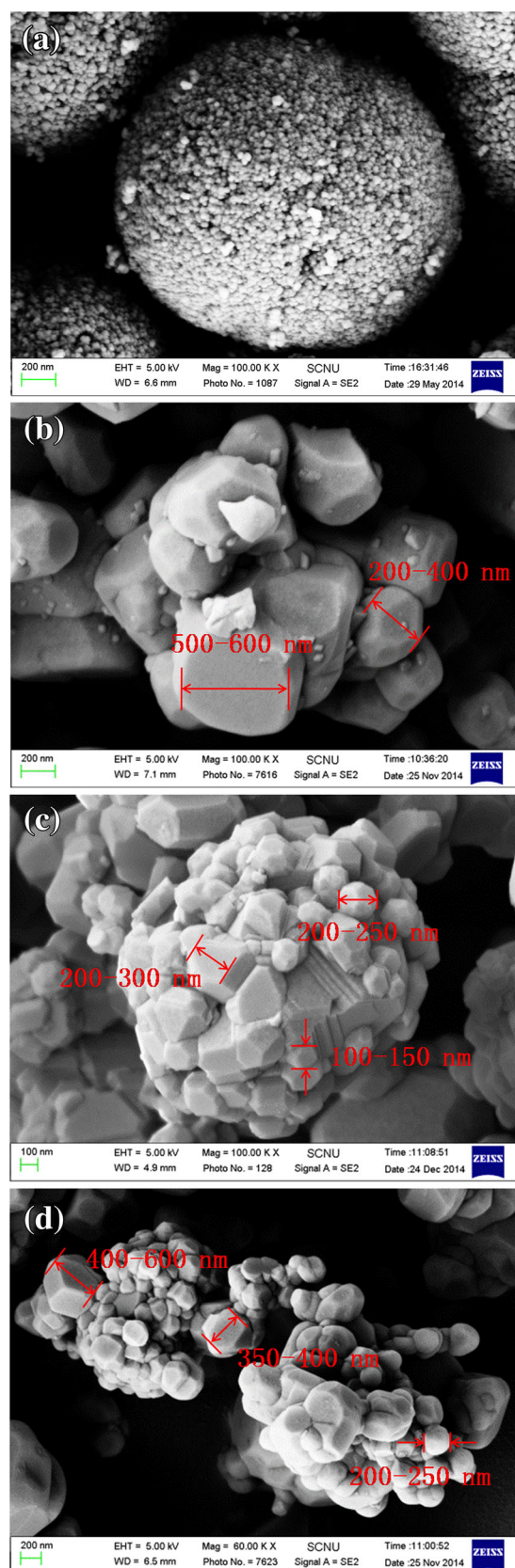
**Fig. 1** XRD patterns of the precursor (a) and the  $\text{Li}_{1+x}(\text{Mn}_{0.6}\text{Ni}_{0.2}\text{Co}_{0.2})_{1-x}\text{O}_2$  materials ( $x = 0.14, 0.165, 0.19$ ) (b)

20 $^{\circ}$  and 25 $^{\circ}$  reflect a hexagonal  $\alpha\text{-NaFeO}_2$  layered structure with  $R-3m$  space group [13, 35, 36]. The small superlattice peaks observed between 20 $^{\circ}$  and 25 $^{\circ}$  represent the existence of monoclinic  $\text{Li}_2\text{MnO}_3$  phase with  $C2/m$  space group [37], conforming to the  $\text{LiMn}_6$  cation arrangement in the transition metal layers of the extremely small  $\text{Li}_2\text{MnO}_3$  regions [9]. Obviously, the weak peaks become symmetrical and sharp with the decrease of  $x$ . The distinct splitting peaks of (006)/(102) and (108)/(110) indicate that the Li-rich cathode materials exhibit a well-formed layered hexagonal structure and high crystallinity. No any impurity peak is detected, suggesting the high purity of the oxides. With respect to the formation of  $\text{Li}_{1+x}(\text{Mn}_{0.6}\text{Ni}_{0.2}\text{Co}_{0.2})_{1-x}\text{O}_2$  ( $x = 0.14, 0.165, 0.19$ ), all samples present small differences in the sharpness and position of the peaks. Besides, as can be seen from Fig. 1b, the peaks shift slightly toward higher  $2\theta$  values from  $x = 0.14$  to  $x = 0.19$ , which may be ascribed to the bigger ion radius of  $\text{Li}^+$  (0.68  $\text{\AA}$ ) than  $\text{Mn}^{4+}$  (0.60  $\text{\AA}$ ) and  $\text{Co}^{3+}$  (0.63  $\text{\AA}$ ) [38].

The morphologies of the precursor and composites are investigated by SEM in Fig. 2. As shown in Fig. 2a, the precursor presents a spherical shape with small particle size (2  $\mu\text{m}$ ). Figure 2b–d show the morphologies of the three samples ( $x = 0.14, 0.165, 0.19$ ), respectively, after high-temperature solid-state reaction. Apparently, the spherical shape is well maintained for the sample  $\text{Li}_{1.165}\text{Mn}_{0.501}\text{Ni}_{0.167}\text{Co}_{0.167}\text{O}_2$  ( $x = 0.165$ ) after calcination process owing to surface force, distinctly accompanying with the formation of layered structure, while the shapes of the  $\text{Li}_{1.14}\text{Mn}_{0.516}\text{Ni}_{0.172}\text{Co}_{0.172}\text{O}_2$  ( $x = 0.14$ ) and  $\text{Li}_{1.19}\text{Mn}_{0.486}\text{Ni}_{0.162}\text{Co}_{0.162}\text{O}_2$  ( $x = 0.19$ ) are irregular but have the trend of agglomerating to spheres. The average diameters of the primary particles of the three samples ( $x = 0.14, 0.165, 0.19$ ) are determined to be about 200–600, 100–300, and 200–600 nm, respectively. The secondary particles of the  $\text{Li}_{1.165}\text{Mn}_{0.501}\text{Ni}_{0.167}\text{Co}_{0.167}\text{O}_2$  have a bigger size (about 1.8  $\mu\text{m}$ ) owing to agglomeration. Comparatively speaking, the  $\text{Li}_{1.165}\text{Mn}_{0.501}\text{Ni}_{0.167}\text{Co}_{0.167}\text{O}_2$  is well shaped with smooth surfaces and sharp edges and has uniform particle size distribution, which is believed to be beneficial to shorten the  $\text{Li}^+$  diffusion distance and increase specific surface areas and facilitate the Li insertion/extraction; thus, it is advantageous for the depth of the charge and discharge and enhance the electrochemical reaction activity.

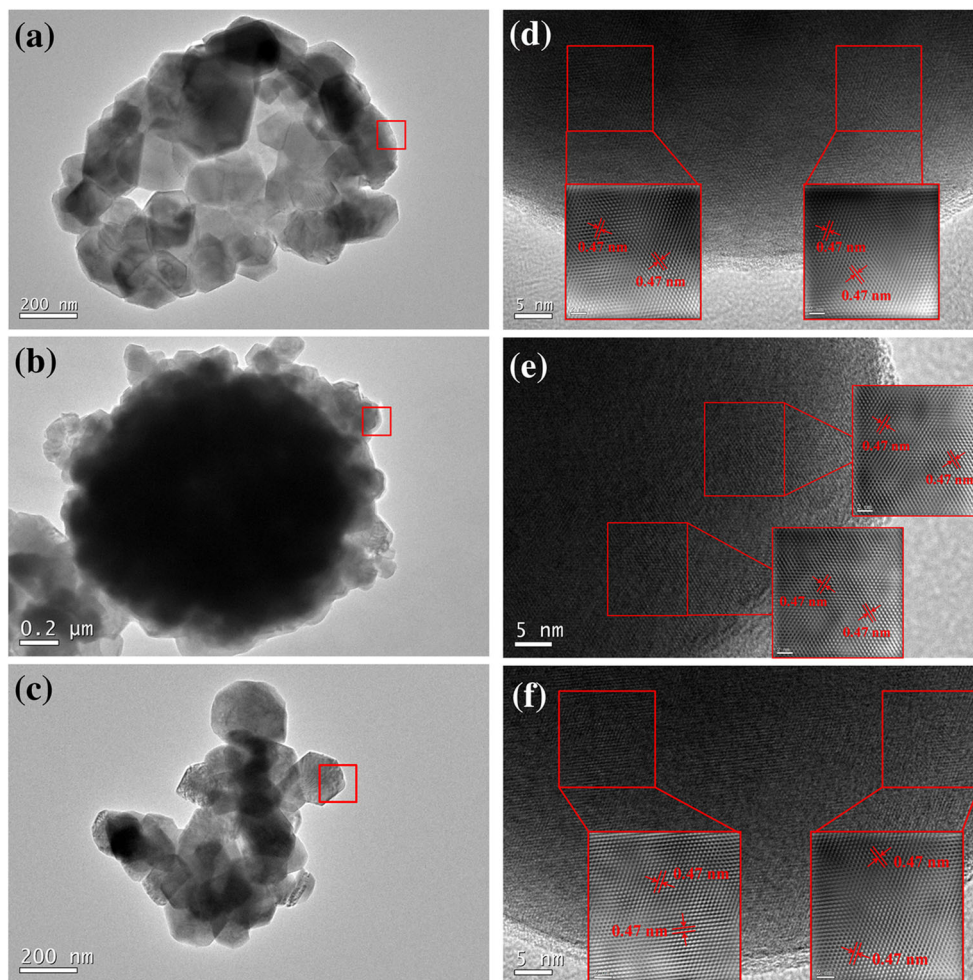
The microstructure of the as-prepared  $\text{Li}_{1+x}(\text{Mn}_{0.6}\text{Ni}_{0.2}\text{Co}_{0.2})_{1-x}\text{O}_2$  ( $x = 0.14, 0.165, 0.19$ ) was explored by transmission electron microscopy (TEM). The TEM images (Fig. 3a–c) could indicate the morphology and particle size. As can be seen from Fig. 3b, the TEM image of the  $\text{Li}_{1.165}\text{Mn}_{0.501}\text{Ni}_{0.167}\text{Co}_{0.167}\text{O}_2$  presents regularly agglomerated spherical shapes with a size of 1.8  $\mu\text{m}$  in diameter, which is consistent with the SEM images of Fig. 2c. Figure 3d–f shows the HRTEM images of the selected area in Fig. 3a–c, respectively. The HRTEM image of the  $\text{Li}_{1.165}\text{Mn}_{0.501}\text{Ni}_{0.167}\text{Co}_{0.167}\text{O}_2$  in Fig. 3e exhibits distinct parallel lattice fringes, while the lattice fringes of  $\text{Li}_{1.14}\text{Mn}_{0.516}\text{Ni}_{0.172}\text{Co}_{0.172}\text{O}_2$  and  $\text{Li}_{1.19}\text{Mn}_{0.486}\text{Ni}_{0.162}\text{Co}_{0.162}\text{O}_2$  cannot distinguish clearly in Fig. 3d, f. According to our previous studies [30], the atomic arrangement tends to be in good order due to atomic diffusion during the high-temperature calcination process, forming a complete crystal structure. Relatively speaking, it is considered that  $\text{Li}_{1.165}\text{Mn}_{0.501}\text{Ni}_{0.167}\text{Co}_{0.167}\text{O}_2$  exhibits better crystallization. About 0.47 nm of the interplanar spacing between two lattice fringes can be measured, which corresponds to (003) planes from rhombohedral phase with  $R\bar{3}m$  space group or (001) planes from monoclinic phase with  $C2/m$  space group [22]. It is consistent with the above XRD analysis.

Figure 4a presents the cycling performance of the as-prepared materials at a current density of 25  $\text{mA g}^{-1}$  (0.1 C) between 2.0 and 4.65 V. All of the three samples display excellent cycle performance with high capacity retention. As shown in Fig. 4a, the charge/discharge capacity has a



**Fig. 2** SEM images of the precursor (a) and the  $\text{Li}_{1+x}(\text{Mn}_{0.6}\text{Ni}_{0.2}\text{Co}_{0.2})_{1-x}\text{O}_2$  materials:  $x = 0.14$  (b),  $x = 0.165$  (c),  $x = 0.19$  (d)

**Fig. 3** TEM and HRTEM images of the  $\text{Li}_{1+x}(\text{Mn}_{0.6}\text{Ni}_{0.2}\text{Co}_{0.2})_{1-x}\text{O}_2$ :  $x = 0.14$  (a, d),  $x = 0.165$  (b, e),  $x = 0.19$  (c, f)



gradually decreased trend for the following cycles. Moreover, the coulombic efficiencies of all samples are mostly over 98.0 % during the following cycles. Herein, the  $\text{Li}_{1.14}\text{Mn}_{0.516}\text{Ni}_{0.172}\text{Co}_{0.172}\text{O}_2$  ( $x = 0.14$ ) and  $\text{Li}_{1.19}\text{Mn}_{0.486}\text{Ni}_{0.162}\text{Co}_{0.162}\text{O}_2$  ( $x = 0.19$ ) deliver an initial discharge capacity of  $194.7 \text{ mAh g}^{-1}$  and  $198.4 \text{ mAh g}^{-1}$ , respectively, revealing the corresponding initial coulombic efficiency of 63.6 and 69.6 %. And the discharge capacities of  $194.0$  and  $179.2 \text{ mAh g}^{-1}$  can be obtained after 100 cycles for the  $\text{Li}_{1.14}\text{Mn}_{0.516}\text{Ni}_{0.172}\text{Co}_{0.172}\text{O}_2$  and  $\text{Li}_{1.19}\text{Mn}_{0.486}\text{Ni}_{0.162}\text{Co}_{0.162}\text{O}_2$ , respectively. Comparatively speaking, the  $\text{Li}_{1.165}\text{Mn}_{0.501}\text{Ni}_{0.167}\text{Co}_{0.167}\text{O}_2$  delivers the highest initial charge and discharge capacity of  $344.0$  and  $241.7 \text{ mAh g}^{-1}$ , respectively, indicating a high initial coulombic efficiency of 70.3 %. Moreover, its discharge capacity of  $207.2 \text{ mAh g}^{-1}$  is still maintained after 100 cycles. Such high specific capacity and cycling stability are mainly attributed to well-formed structure and uniform particle size, making for the  $\text{Li}^+$  extraction and shortening of the  $\text{Li}^+$  diffusion distance. In addition, it can be obviously seen from the figure that the capacity of the  $\text{Li}_{1.19}\text{Mn}_{0.486}\text{Ni}_{0.162}\text{Co}_{0.162}\text{O}_2$  increases gradually in the first

10 cycles until reaching a stable point, which may be caused by the electrochemical activation process of the battery.

Figure 4b reveals the rate capability of the as-prepared materials from 0.1 C to 10 C between 2.0 and 4.65 V. For the  $\text{Li}_{1.14}\text{Mn}_{0.516}\text{Ni}_{0.172}\text{Co}_{0.172}\text{O}_2$ , the discharge capacities of  $210.8, 190.2, 161.0, 139.9, 111.1, 87.7,$  and  $52.2 \text{ mAh g}^{-1}$  can be obtained at 0.1 C, 0.2 C, 0.5 C, 1 C, 2 C, 5 C, and 10 C, respectively. The delivered capacities of the  $\text{Li}_{1.19}\text{Mn}_{0.486}\text{Ni}_{0.162}\text{Co}_{0.162}\text{O}_2$  at 0.1 C, 0.2 C, 0.5 C, 1 C, 2 C, 5 C, and 10 C are about  $190.8, 172.4, 142.2, 110.2, 80.4, 64.2,$  and  $46.2 \text{ mAh g}^{-1}$ , respectively. With respect to the  $\text{Li}_{1.165}\text{Mn}_{0.501}\text{Ni}_{0.167}\text{Co}_{0.167}\text{O}_2$ , the discharge capacities of  $226.8, 194.4, 158.9, 143.7, 116.8, 97.5,$  and  $47.6 \text{ mAh g}^{-1}$  are attained at 0.1 C, 0.2 C, 0.5 C, 1 C, 2 C, 5 C, and 10 C, respectively. And when the current goes back to 0.1 C, the discharge capacity reaching up to  $224.7 \text{ mAh g}^{-1}$  still can be achieved for the  $\text{Li}_{1.165}\text{Mn}_{0.501}\text{Ni}_{0.167}\text{Co}_{0.167}\text{O}_2$ . Therefore, the  $\text{Li}_{1.165}\text{Mn}_{0.501}\text{Ni}_{0.167}\text{Co}_{0.167}\text{O}_2$  exhibits better rate capability due to its small primary particle size and large specific surface areas, decreasing ion diffusion distance and contributing to the  $\text{Li}^+$  extraction during the charge/discharge process. All samples reflect a gradual loss of the capacity with the

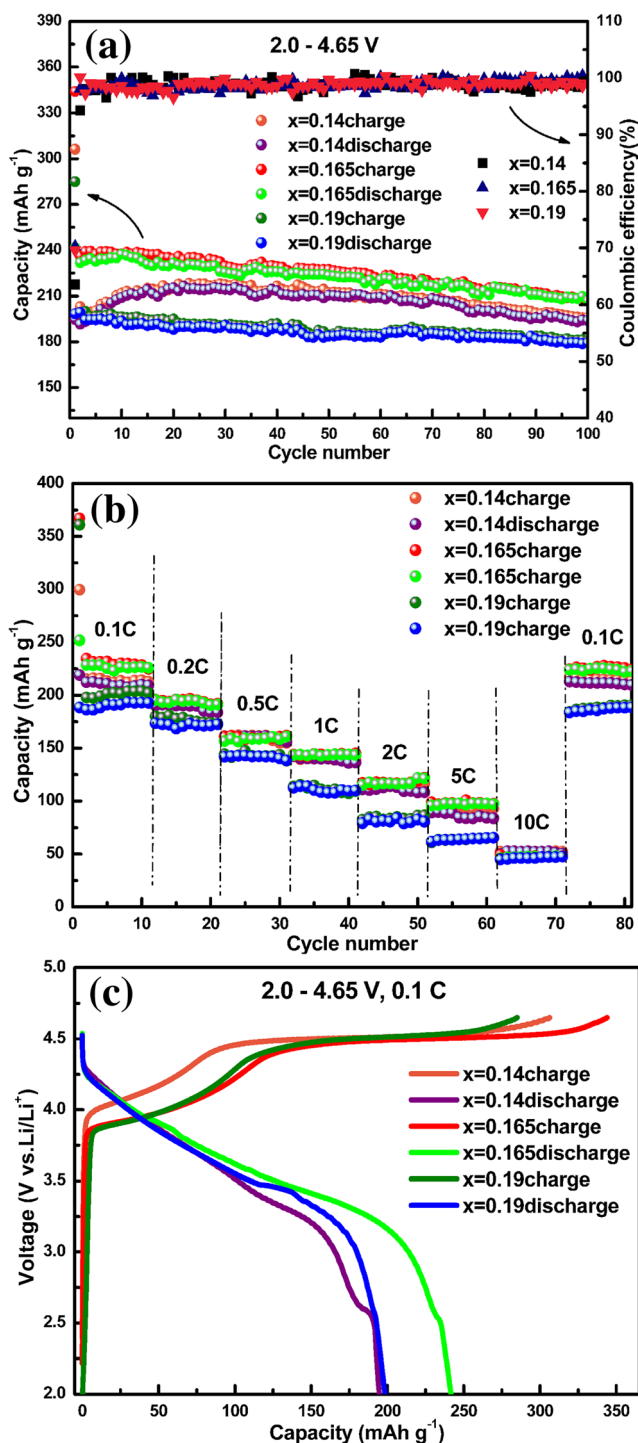


**Fig. 4** Cycle performance (a), rate capability (b), and initial charge-discharge curves (c) of the  $\text{Li}_{1+x}(\text{Mn}_{0.6}\text{Ni}_{0.2}\text{Co}_{0.2})_{1-x}\text{O}_2$  materials ( $x = 0.14, 0.165, 0.19$ ) between 2.0 and 4.65 V

increasing of the current densities. The decrease is mainly ascribed to the lattice disorders at high rates [9]; thus, the extraction of  $\text{Li}^+$  is hindered, producing high polarization and capacity attenuation.

The initial charge-discharge curves of three samples at 0.1 C between 2.0 and 4.65 V are displayed in Fig. 4c. Two charge

plateaus in the initial charge process can be seen from the graph. The first one at 3.9–4.5 V is relative to the delithiation of  $\text{LiMO}_2$  phase accompanied with the oxidation of  $\text{Ni}^{2+} \rightarrow \text{Ni}^{4+}$  and  $\text{Co}^{3+} \rightarrow \text{Co}^{4+}$ . The second one, which is located above 4.5 V, embodies the extraction of  $\text{Li}_2\text{O}$  from the layered  $\text{Li}_2\text{MnO}_3$  lattice producing a high irreversible charge capacity simultaneously [22]. As can be clearly observed, the charge and discharge capacities in the first cycle in Fig. 4c are completely consistent with what Fig. 4a depicts, equally demonstrating the outstanding electrochemical performance of the  $\text{Li}_{1.165}\text{Mn}_{0.501}\text{Ni}_{0.167}\text{Co}_{0.167}\text{O}_2$  compared with the  $\text{Li}_{1.14}\text{Mn}_{0.516}\text{Ni}_{0.172}\text{Co}_{0.172}\text{O}_2$  and  $\text{Li}_{1.19}\text{Mn}_{0.486}\text{Ni}_{0.162}\text{Co}_{0.162}\text{O}_2$ . Apparently, an abnormal plateau at 2.6 V is newly formed for the  $\text{Li}_{1.14}\text{Mn}_{0.516}\text{Ni}_{0.172}\text{Co}_{0.172}\text{O}_2$  and  $\text{Li}_{1.165}\text{Mn}_{0.501}\text{Ni}_{0.167}\text{Co}_{0.167}\text{O}_2$ , which is usually considered to be a sign of spinel formation [39].

Electrochemical impedance spectroscopy (EIS) has been measured to deeply study the electrochemical performance. The Nyquist plots of EIS spectra for these composites at the charge state of 4.65 V after 100 cycles are shown in Fig. 5a. The plots consist of a semicircle in the high frequency, a semicircle in the intermediate frequency, and a tail in the low frequency. Generally, the high-frequency semicircle is assigned to the solid electrolyte interface (SEI) resistance ( $R_f$ ) of  $\text{Li}^+$  diffusion in the passive SEI layer, which is formed due to the oxidation of electrolyte accompanying the formation of  $\text{Li}_2\text{CO}_3$  during the electrochemical activation of  $\text{Li}_2\text{MnO}_3$  [17, 40]. The intermediate-frequency semicircle is ascribed to the charge transfer electrochemical resistance ( $R_{ct}$ ) of the electrode/electrolyte interface. Nevertheless, the lattice rearrangement process during cycling can result in a disordered surface structure, and thus, the charge transfer especially for  $\text{Li}^+$  suffers obstructions [17]. The low-frequency tail is associated with the Warburg impedance ( $Z_w$ ) of the  $\text{Li}^+$  diffusion in the solid-phase active material. When the slope of this line is bigger, the impedance is smaller on the contrary, suggesting an easier diffusion. Comparing the three magnified curves in the magnified inset of Fig. 5a, the  $\text{Li}_{1.14}\text{Mn}_{0.516}\text{Ni}_{0.172}\text{Co}_{0.172}\text{O}_2$  and  $\text{Li}_{1.165}\text{Mn}_{0.501}\text{Ni}_{0.167}\text{Co}_{0.167}\text{O}_2$  perform the smaller radius of the high frequency far less than that of the  $\text{Li}_{1.19}\text{Mn}_{0.486}\text{Ni}_{0.162}\text{Co}_{0.162}\text{O}_2$ , illustrating a smaller interfacial film impedance and easier  $\text{Li}^+$  diffusion. Figure 5b shows the equivalent circuit of the Nyquist plots.  $R_e$ ,  $CPE_f$ , and  $CPE_{ct}$  stand for the solution impedance, non-ideal capacitance of the surface layer, and non-ideal capacitance of the double layer, respectively [9, 13]. The fitting results of  $R_e$ ,  $R_f$  and  $R_{ct}$  are listed in Table 1. Obviously, the  $\text{Li}_{1.165}\text{Mn}_{0.501}\text{Ni}_{0.167}\text{Co}_{0.167}\text{O}_2$  ( $x = 0.165$ ) owns the lowest impedance, suggesting superior electrochemical performance as compared with the other two samples.

Based on the above-mentioned analysis, the  $\text{Li}_{1.165}\text{Mn}_{0.501}\text{Ni}_{0.167}\text{Co}_{0.167}\text{O}_2$  exhibits the best electrochemical performance; thus, its cyclic voltammetry (CV) test is performed

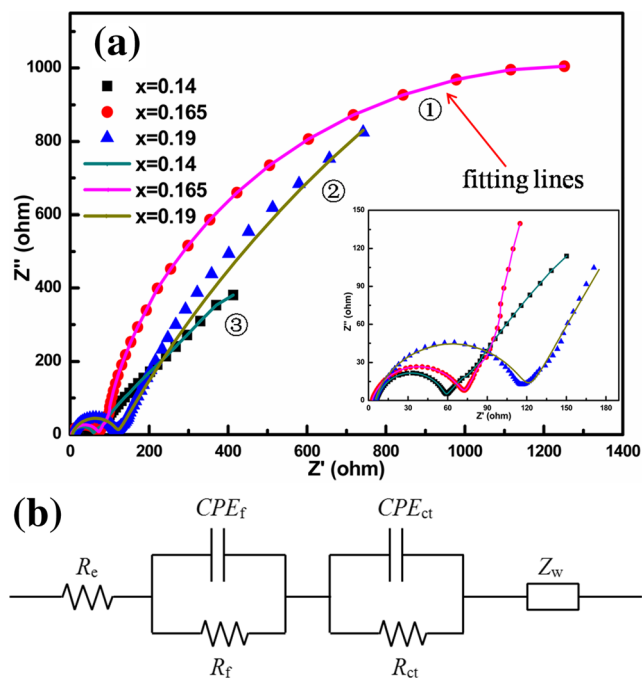


**Fig. 5** Nyquist plots (a) of the  $\text{Li}_{1+x}(\text{Mn}_{0.6}\text{Ni}_{0.2}\text{Co}_{0.2})_{1-x}\text{O}_2$  materials ( $x = 0.14, 0.165, 0.19$ ) and equivalent circuit (b) performed to fit the curves

to acquire deep insights into the electrochemical behavior during the charge/discharge process. Figure 6a displays the CV curves of the  $\text{Li}_{1.165}\text{Mn}_{0.501}\text{Ni}_{0.167}\text{Co}_{0.167}\text{O}_2$  in the first three cycles at a scan rate of  $0.1 \text{ mV s}^{-1}$  in the voltage range of 2.5–4.65 V. The curves in the initial cycle are sharp, symmetrical, and accordant with what are shown in the initial charge-discharge curves. Two main sharp oxidation peaks in the charging state can be discerned in the initial cycle, located at 4.14 and 4.63 V, respectively. The first oxidation peak located at 4.14 V corresponds to the extraction of  $\text{Li}^+$  from the  $\text{LiMO}_2$  structure along with the oxidation of  $\text{Ni}^{2+}$  to  $\text{Ni}^{4+}$  and  $\text{Co}^{3+}$  to  $\text{Co}^{4+}$ . It is worthy to point out that the excessive Li will begin to extract from the  $\text{Li}_2\text{MnO}_3$  phase when charged above 4.4 V [13], so the activation peaks at the high potential 4.63 V, which become weaker with the increase of cycle number, are ascribed to the activation of  $\text{Li}_2\text{MnO}_3$  component and the loss of oxygen. What is more, three reduction peaks are discernable at 3.3, 3.8, and 4.4 V. Therein, the reduction peak at 3.3 V can be clearly observed especially in the second and third cycles, which is attributed to the reduction reaction of  $\text{Mn}^{4+}$  due to the loss of oxygen in the first charge. The other two reduction peaks at 3.8 and 4.4 V are related to the  $\text{Li}^+$

**Table 1** The fitting results of equivalent circuit of the  $\text{Li}_{1+x}(\text{Mn}_{0.6}\text{Ni}_{0.2}\text{Co}_{0.2})_{1-x}\text{O}_2$  ( $x = 0.14, 0.165, 0.19$ )

$x$	$R_e$	$R_f$	$R_{ct}$
0.14	6.10	53.45	6182
0.165	2.89	70.01	2765
0.19	5.35	114.7	5438

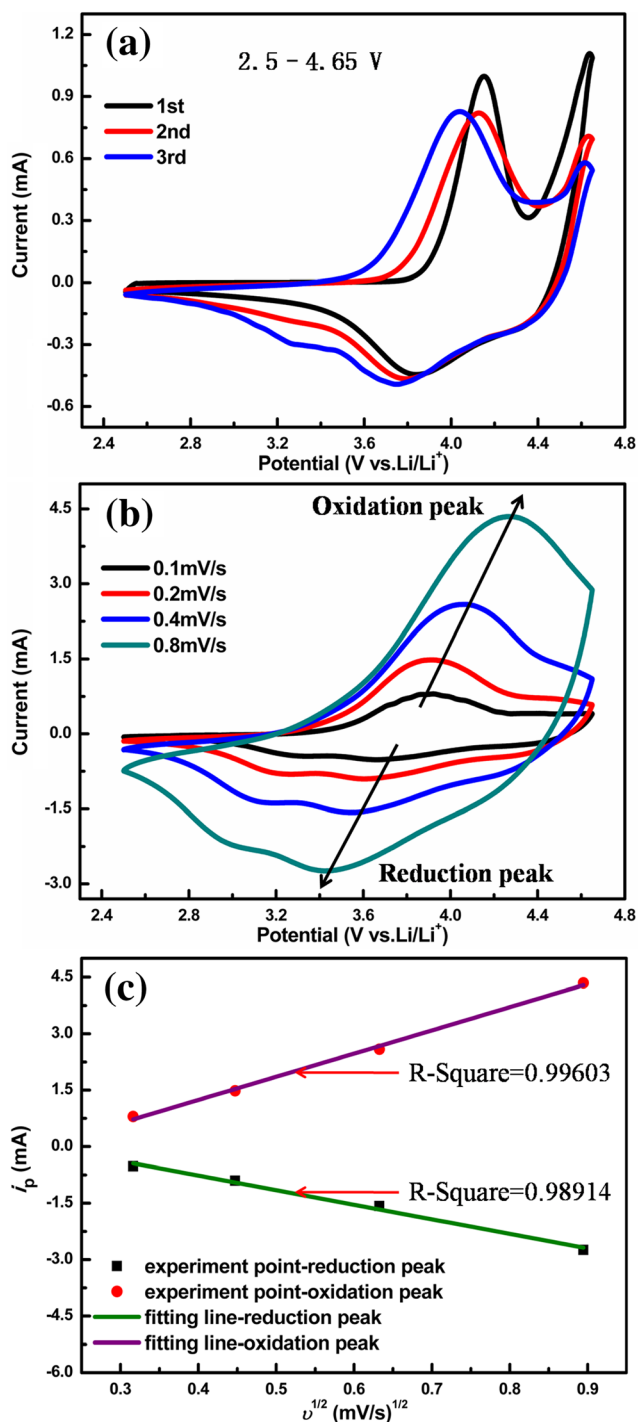


**Fig. 6** CV curves of the  $\text{Li}_{1.165}\text{Mn}_{0.501}\text{Ni}_{0.167}\text{Co}_{0.167}\text{O}_2$  ( $x = 0.165$ ) between 2.5 and 4.65 V: at the scan rate of  $0.1 \text{ mV s}^{-1}$  (a); at different scan rates of 0.1, 0.2, 0.4, and  $0.8 \text{ mV s}^{-1}$  (b). The current of peaks ( $i_p$ ) vs the square root of scanning rates ( $v^{1/2}$ ) plots (c) of the  $\text{Li}_{1.165}\text{Mn}_{0.501}\text{Ni}_{0.167}\text{Co}_{0.167}\text{O}_2$

reinsertion to  $\text{LiM}_{1-x}\text{O}_2$  phase accompanying the reduction of  $\text{Ni}^{4+}$  to  $\text{Ni}^{2+}$  and  $\text{Co}^{4+}$  to  $\text{Co}^{3+}$  [41]. The reduction peaks at 3.8 and 4.4 V are highly overlapped, demonstrating a fairly well cyclic reversibility. The redox peaks have the trend of

shifting to lower potential, which is due to the modification of the bulk material structure after the first cycle or the oxidation of  $\text{Co}^{3+}$  to  $\text{Co}^{4+}$  and part of the electrolyte [42, 43], and it means a smaller potential difference between oxidation peak and reduction peak, indicating the smaller polarization effect.

The improved rate capability of the  $\text{Li}_{1.165}\text{Mn}_{0.501}\text{Ni}_{0.167}\text{Co}_{0.167}\text{O}_2$  can also be explained by means of CV analysis. Figure 6b shows the CV curves of the  $\text{Li}_{1.165}\text{Mn}_{0.501}\text{Ni}_{0.167}\text{Co}_{0.167}\text{O}_2$  at different scan rates between 2.5 and 4.65 V. As clearly indicated, the oxidation peaks move to higher potentials, while the reduction peaks move to lower potentials with the increase of scan rate. In addition, the area surrounded by the oxidation peak and reduction peak is significantly increased with the increase of scan rate. Figure 6c shows the current of peaks ( $i_p$ ) vs the square root of scanning rates ( $v^{1/2}$ ) plots of the  $\text{Li}_{1.165}\text{Mn}_{0.501}\text{Ni}_{0.167}\text{Co}_{0.167}\text{O}_2$ . The lithium-ion diffusion coefficient of the  $\text{Li}_{1.165}\text{Mn}_{0.501}\text{Ni}_{0.167}\text{Co}_{0.167}\text{O}_2$  ( $x = 0.165$ ) can be calculated as the following equation:

$$i_p = (2.69 \times 10^5) n^{3/2} A D_{\text{Li}^+}^{1/2} C v^{1/2}$$

where  $n$  is the electron transfer numbers of redox reactions ( $n = 1$ ),  $A$  is the effective surface area of the electrode ( $2.54 \text{ cm}^2$ ),  $D_{\text{Li}^+}$  is the lithium-ion diffusion coefficient,  $C$  is the molar concentration of lithium-ion ( $9.8975 \times 10^{-2} \text{ mol cm}^{-3}$ ), and  $v$  is the scan rates. It can be calculated for the  $\text{Li}_{1.165}\text{Mn}_{0.501}\text{Ni}_{0.167}\text{Co}_{0.167}\text{O}_2$  ( $x = 0.165$ ) that the lithium-ion diffusion coefficient of the oxidation and reduction peaks are  $8.30946 \times 10^{-9}$  and  $3.27828 \times 10^{-9} \text{ cm}^2 \text{ s}^{-1}$ , respectively. Besides, the R-square of the fitting lines and the accuracy rating of the calculated diffusion coefficient of oxidation and reduction peaks are 0.99603 and 0.98914, respectively, indicating a low error and high reliability of the fitting data.

## Conclusions

The  $\text{Li}_{1+x}(\text{Mn}_{0.6}\text{Ni}_{0.2}\text{Co}_{0.2})_1 - x\text{O}_2$  ( $x = 0.14, 0.165, 0.19$ ) cathode materials were successfully synthesized by a one-pot facile co-precipitation method. The impact of lithium content on the electrochemical properties was mainly discussed. It comes to a conclusion that the  $\text{Li}_{1.165}\text{Mn}_{0.501}\text{Ni}_{0.167}\text{Co}_{0.167}\text{O}_2$  ( $x = 0.165$ ) exhibits an outstanding electrochemical performance in terms of cycling stability and rate capability. Its charge- and discharge-specific capacity of 344.0 and 241.7  $\text{mAh g}^{-1}$  can be achieved in the first cycle at 0.1 C (1 C = 250  $\text{mA g}^{-1}$ ), and the discharge capacity of 207.2  $\text{mAh g}^{-1}$  is still maintained after 100 cycles. Furthermore, the discharge capacities of approximately 226.8, 194.4, 158.9, 143.7, 116.8, 97.5, and 47.6  $\text{mAh g}^{-1}$  can also be attained at 0.1 C, 0.2 C, 0.5 C, 1 C, 2 C, 5 C, and 10 C,

respectively. The superior performance can be ascribed to small particle size and good crystallinity, which can shorten the  $\text{Li}^+$  diffusion distance and increase specific surface areas, facilitating the Li insertion/extraction and enhancing the electrochemical reaction activity. In summary, the Li-rich layered  $\text{Li}_{1.165}\text{Mn}_{0.501}\text{Ni}_{0.167}\text{Co}_{0.167}\text{O}_2$  cathode material with excellent performance will be appealing and alternative for large-scale commercial applications in advanced lithium-ion batteries. On the side, the long-term project concerning lithium content is still urgent to in-depth study to further improve the electrochemical performance of lithium-ion batteries.

**Acknowledgments** This work was financially supported by the National Science Foundation of China (NSFC, Nos. 51201066 and 51171065), the Natural Science Foundation of Guangdong Province (No. S2012020010937), Science and Technology Project Foundation of Zhongshan City of Guangdong Province of China (No. 20123A326), and College Students' Innovative Entrepreneurial Training Program of South China Normal University (No. 2014058).

## References

- Ye DL, Wang B, Chen Y, Han G, Zhang Z, Hulicova-Jurcakova D, Zou J, Wang LZ (2014) *J Mater Chem A* 2:18767–18774
- Noh HJ, Youn S, Yoon CS, Sun YK (2013) *J Power Sources* 233: 121–130
- Harry KJ, Hallinan DT, Parkinson DY, MacDowell AA, Balsara NP (2014) *Nat Mater* 13:69–73
- Yao LM, Hou XH, Hu SJ, Ru Q, Tang XQ, Zhao LZ, Sun DW (2013) *J Solid State Electrochem* 17:2055–2060
- Yu DYW, Prikhodchenko PV, Mason CW, Batabyal SK, Gun J, Sladkevich S, Medvedev AG, Lev O (2013) *Nat Commun* 4: 2922–2929
- Yao YL, Liu HC, Li GC, Peng HR, Chen KZ (2013) *Electrochim Acta* 113:340–345
- Li M, Hou XH, Sha YJ, Wang J, Hu SJ, Liu X, Shao ZP (2014) *J Power Sources* 248:721–728
- Zheng JM, Wu XB, Yang Y (2011) *Electrochim Acta* 56:3071–3078
- Shi SJ, Tu JP, Tang YY, Yu YX, Zhang YQ, Wang XL (2013) *J Power Sources* 221:300–307
- Yu HJ, Zhou HS (2013) *J Phys Chem Lett* 4:1268–1280
- Ebin B, Lindbergh G, Grmen S (2015) *J Alloys Compd* 620:399–406
- Li J, Klpsch R, Stan MC, Nowak S, Kunze M, Winter M, Passerini S (2011) *J Power Sources* 196:4821–4825
- Shi SJ, Tu JP, Tang YY, Zhang YQ, Wang XL, Gu CD (2013) *J Power Sources* 240:140–148
- Riou A, Lecerf A, Gerault Y, Cudennec Y (1992) *Mater Res Bull* 27:269–275
- Strobel P, Lambert-Andron B (1988) *J Solid State Chem* 75:90–98
- Akimoto J, Gotoh Y, Oosawa Y (1998) *J Solid State Chem* 141: 298–302
- Zhang QG, Peng TY, Zhan D, Hu XH (2014) *J Power Sources* 250: 40–49
- Gu M, Ilias Belharouak, Zheng JM, Wu HM, Xiao J, Genc A, Amine K, Thevuthasan S, Baer DR, Zhang JG, Browning ND, Liu J, Wang CM (2013) *ACS Nano* 7:760–767



19. Yang XK, Wang XY, Zou GS, Hu L, Shu HB, Yang SY, Liu L, Hu H, Yuan H, Hu BN, Wei QL, Yi LH (2013) *J Power Sources* 232:338–347
20. Deng YH, Liu SQ, Liang XX (2013) *J Solid State Electrochem* 17: 1067–1075
21. Miao XW, Yan Y, Wang CG, Cui LL, Fang JH, Yang G (2014) *J Power Sources* 247:219–227
22. Wang J, Yuan GX, Zhang MH, Qiu B, Xia YG, Liu ZP (2012) *Electrochim Acta* 66:61–66
23. Min JW, Kalathil AK, Yim CJ, Im WB (2014) *Mater Charact* 92: 118–126
24. Fu F, Deng YP, Shen CH, Xu GL, Peng XX, Wang Q, Xu YF, Fang JC, Huang L, Sun SG (2014) *Electrochem Commun* 44:54–58
25. Liu H, Du CY, Yin GP, Song B, Zuo PJ, Cheng XQ, Ma YL, Gao YZ (2014) *J Mater Chem A* 2:15640–15646
26. Wang J, Lin WQ, Wu BH, Zhao JB (2014) *Electrochim Acta* 145: 245–253
27. Li HX, Fan LZ (2013) *Electrochim Acta* 113:407–411
28. Zhang HZ, Qiao QQ, Li GR, Gao XP (2014) *J Mater Chem A* 2: 7454–7460
29. Xue QR, Li JL, Xu GF, Zhou HW, Wang XD, Kang FY (2014) *J Mater Chem A* 2:18613–18623
30. Hou XH, Zou XL, Huang YL, Hu SJ, Ru Q, Gao YM (2014) *RSC Adv* 4:29534–29541
31. Li Q, Li GS, Fu CC, Luo D, Fan JM, Li LP (2014) *ACS Appl Mater Interfaces* 6:10330–10341
32. Zhang J, Lu QW, Fang JH, Wang JL, Yang J, NuLi YN (2014) *ACS Appl Mater Interfaces* 6:17965–17973
33. Zhang XH, Luo D, Li GS, Zheng J, Yu C, Guan XF, Fu CC, Huang XD, Li LP (2013) *J Mater Chem A* 1:9721–9729
34. Song BH, Lai MO, Liu ZW, Liu HW, Lu L (2013) *J Mater Chem A* 1:9954–9965
35. Toprakci O, Toprakci HAK, Li Y, Ji LW, Xue LG, Lee H, Zhang S, Zhang XW (2013) *J Power Sources* 241:522–528
36. Gao M, Lian F, Liu HQ, Tian CJ, Ma LL, Yang WY (2013) *Electrochim Acta* 95:87–94
37. Zhao TL, Chen S, Li L, Zhang XF, Chen RJ, Belharouak I, Wu F, Amine K (2013) *J Power Sources* 228:206–213
38. Tang ZH, Wang ZX, Li XH, Peng WJ (2012) *J Power Sources* 208: 237–241
39. Song BH, Liu HW, Liu ZW, Xiao PF, Lai MO, Lu L (2013) *Sci Rep* 3:3094–3106
40. Yabuuchi N, Yoshii K, Myung ST, Nakai I, Komaba S (2011) *J Am Chem Soc* 133:4404–4419
41. Manikandan P, Periasamy P, Jagannathan R (2014) *RSC Adv* 4: 40359–40367
42. Wei X, Zhang SC, Du ZJ, Yang PH, Wang J, Ren YB (2013) *Electrochim Acta* 107:549–554
43. Li HF, Pang J, Yin YP, Zhuang WD, Wang H, Zhai CX, Lu SG (2013) *RSC Adv* 3:13907–13914